EMBRY-RIDDLE
Aeronautical University™
SCHOLARLY COMMONS

Publications

3-27-2001

Climatology and Modeling of Quasi-monochromatic Atmospheric Gravity Waves Observed over Urbana Illinois

J. H. Hecht
The Aerospace Corporation

R. L. Walterscheid
The Aerospace Corporation

Michael P. Hickey Ph.D.
Embry-Riddle Aeronautical University, hicke0b5@erau.edu

S. J. Franke
University of Illinois at Urbana-Champaign

Follow this and additional works at: https://commons.erau.edu/publication

Part of the Atmospheric Sciences Commons

Scholarly Commons Citation

Climatology and modeling of quasi-monochromatic atmospheric gravity waves observed over Urbana Illinois

J. H. Hecht and R. L. Walterscheid

Space Science Applications Laboratory, The Aerospace Corporation, Los Angeles, California

M. P. Hickey

Department of Physics and Astronomy, Clemson University, Clemson, South Carolina

S. J. Franke

Department of Electrical and Computer Engineering, University of Illinois, Urbana, Illinois

Abstract. From analyzing nine months of airglow imaging observations of atmospheric gravity waves (AGWs) over Adelaide, Australia (35°S) [*Walterscheid et al.*, 1999] have proposed that many of the quasi-monochromatic waves seen in the images were primarily thermally ducted. Here are presented 15 months of observations, from February 1996 to May 1997, for AGW frequency and propagation direction from a northern latitude site, Urbana Illinois (40°N). As Adelaide, Urbana is geographically distant from large orographic features. Similar to what was found in Adelaide, the AGWs seem to originate from a preferred location during the time period around summer solstice. In conjunction with these airglow data there exists MF radar data to provide winds in the 90 km region and near-simultaneous lidar data which provide a temperature climatology. The temperature data have previously been analyzed by *States and Gardner* [2000]. The temperature and wind data are used here in a full wave model analysis to determine the characteristics of the wave ducting and wave reflection during the 15 month observation period. This model analysis is applied to this and another existing data set recently described by *Nakamura et al.* [1999]. It is shown that the existence of a thermal duct around summer solstice can plausibly account for our observations. However, the characteristics of the thermal duct and the ability of waves to be ducted is also greatly dependent on the characteristics of the background wind. A simple model is constructed to simulate the trapping of these waves by such a duct. It is suggested that the waves seen over Urbana originate no more than a few thousand kilometers from the observation site.

1. Introduction

The ducting or trapping of atmospheric gravity waves (AGWs) has long been a subject of interest [e.g., *Pitteway and Hines*, 1965; *Friedman*, 1966; *Francis*, 1973, 1974; *Tuan and Tadic*, 1982; *Chimonas and Hines*, 1986; *Wang and Tuan*, 1988; *Fritts and Yuan*, 1989]. Most of these studies are theoretical, and the initial motivation [*Friedman*, 1966] was to determine if AGWs are the source of traveling ionospheric disturbances (TIDs). These TIDs are observed in the F region and often have horizontal phase speeds well exceeding 100 m/s. Some of these studies considered the existence of ducts caused by thermal gradients or variations in the background winds causing Doppler ducts [e.g., *Chimonas and Hines*, 1986].

However, the advent of CCD imagers has allowed observations of AGWs with different characteristics. These are small-scale waves seen in the airglow layers between 80 and 105 km and which have observed horizontal phase speeds much less than 100 m/s and periods typically less than a few tens of minutes [e.g., *Taylor et al.*, 1995a, 1995b; *Wu and Killeen*, 1996; *Hecht et al.*, 1997; *Walterscheid et al.*, 1999; *Nakamura et al.*,

1999]. The *Taylor et al.* [1995b] study suggested that one of the two observed AGWs was ducted. Some of the more recent modeling efforts cited above [e.g., *Chimonas and Hines*, 1986; *Wang and Tuan*, 1988] postulated that short-period AGWs may be ducted due to a combination of thermal and Doppler ducting. In this modeling study the duct was often bounded by the ground and some altitude in the lower thermosphere.

The study by *Isler et al.* [1997] used simultaneous imager observations of AGWs and MF radar wind data, obtained between 80 and 100 km, to argue that sometimes Doppler wave ducts form because of the variation of the background wind. These ducts are regions of free wave propagation bounded by regions of evanescence produced by wind variations. They argued that many of the waves seen in imager data are trapped by such ducts and are able to travel much farther from the wave source region than would be expected for freely propagating waves based on their horizontal wavelength and period. However, the transient nature of the wind variations observed by *Isler et al.* [1997] suggests that such Doppler ducts are short-lived and perhaps quite local.

The AGWs seen in imagers are also referred to as quasi-monochromatic (QM) waves since one or more cycles of coherent structures are often seen to propagate horizontally across an image. QM waves are waves that typically have horizontal wavelengths of up to a few tens of kilometers and

periods of typically between 5 and 20 min. When freely propagating and not ducted or trapped, these waves would be expected to travel only a few hundred kilometers from their source in the troposphere to where they are observed near the mesopause in airglow observations. One of the reasons for that is that to be seen in the airglow layer, the waves are thought to have vertical wavelengths of nominally 10 km or greater. Thus short-period QM waves should reach the airglow layer of the order of seven wave periods. For a nominal wave period of 10 min and a nominal horizontal wavelength of 30 km this suggests the AGW originated a horizontal distance of the order of 200 km from the observation site.

Recently, *Walterscheid et al.* [1999] have proposed that many of the QM waves seen in airglow imager data may be ducted or trapped in a manner different than the pure Doppler ducts discussed by *Isler et al.* [1997]. The data analyzed by *Walterscheid et al.* [1999] were obtained from 9 months of airglow images obtained over Adelaide, Australia, at 35°S. These data showed a large increase in wave occurrence around summer solstice with a distinct anisotropy in wave propagation directions; the waves appeared to originate from north of Adelaide. However, Adelaide is in a region where there are no large orographic features, and around summer solstice it is quite dry. *Walterscheid et al.* [1999] suggested the only viable source region was several thousand kilometers away over northern Australia coast where intense convective activity occurs at that time of year. If the waves were associated with such distant sources, they must be ducted to reach Adelaide. *Walterscheid et al.* [1999] explored this possibility, using a full wave model analysis [*Hickey et al.*, 1997, 1998] and showed that there exists a lower thermospheric thermal duct, the upper boundary of which occurs around 140 km and the lower boundary being determined by the location of the mesopause. Since the mesopause occurs near 85 km altitude in summer and around 100 km altitude in winter, this would explain why QM wave activity increased in the summer, as such waves were ducted in the airglow layer. In addition, since the waves were observed from the north, they would not be affected by the large eastward or westward mesospheric wind jets, which would either prevent QM waves from entering the thermal duct or cause them to dissipate as critical layers were encountered. The data described by *Walterscheid et al.* [1999] however only covered 9 months, and complete wind and temperature data were not available.

Here we discuss a more extensive data set obtained from 15 months of airglow observations at Urbana, Illinois. Since Urbana is located at 40°N and also far removed from significant orographic features, the location is somewhat a Northern Hemisphere analog to Adelaide, with respect to AGW sources, even though one is on the coast and one is an interior site. In addition to the airglow observations there also exists a climatology of MF radar winds covering the 60 to 100 km altitude region and a recently published climatology of lidar temperatures [*States and Gardner*, 2000] covering the 80 to 105 km region. Portions of both climatologies were obtained during the airglow observation period. The existence of these additional data allows more complete modeling to be performed. Specifically, a full wave model analysis for wave propagation is made with the goal of determining if a wave duct region exists for many directions of propagation, including north, south, east, west, northeast, and southwest. In the *Walterscheid et al.* [1999] work the effects of winds were only considered in detail for eastward and westward propagating waves. In this work we

consider the existence of a combined thermal/Doppler duct for many directions of propagation.

In addition to this new set of observations there has recently been published a wave climatology from Japan at nearly the same latitude as Urbana [*Nakamura et al.*, 1999]. The Urbana and Japanese data sets are compared, and the implications of the full wave model analysis are discussed with respect to both.

The remaining parts of the paper are divided as follows: Section 2 discusses the instrumentation and technique as well as the model. Section 3 presents the results from Urbana and presents a comparison with the Japanese data set and the full wave model analysis. Section 4 presents the discussion of the data and some additional implications of the model and data. Section 5 presents the conclusions.

2. Experimental Instrumentation and Technique

The same airglow imager used by *Walterscheid et al.* [1999] obtained the data in Urbana. This instrument can provide OH Meinel (6, 2) (hereinafter referred to as OHM) and O2 Atmospheric (0, 1) (hereinafter O2A) band images every 7 min. The imager has a field of view (FOV) of around 90 km, at an altitude of 90 km, and thus is sensitive to horizontal wavelengths of QM waves which are of the order of or less than the FOV. The OHM emission originates from a nominally 8 km thick layer centered around 87 km [*She and Lowe*, 1998; *Hecht et al.*, 1998], while the O2A band emission originates from a nominally 10 km thick layer centered a few kilometers below 95 km [*Hecht et al.*, 1997, 1998]. The imager was deployed at Urbana from February 1996 to May 1997. As in the work of *Walterscheid et al.* [1999], a simple wave counting technique was employed. Approximately 40,000 OHM and O2A images were examined. Of these, about 9500 were cloud free. If a wave was seen on an image, it was counted, and its direction of propagation was noted. The direction of propagation over 360° was separated into eight 45° octants. The 15 month period was separated into eight 2 month periods. For each period the total number of images and the fraction, which had waves, was noted, and then the fraction in each octant was plotted.

Nearly simultaneous temperature data were obtained from the University of Illinois Na lidar system. These data were obtained to produce a temperature climatology over Urbana. More than 1000 hours of temperature measurements were made from February 1996 to January 1998. They have been published by *States and Gardner* [2000], and they cover the altitude region from 80 to 105 km. Plots of these temperature profiles as a function of a week of the year are available in the work *States and Gardner* [2000].

Wind data were obtained from the University of Illinois MF radar. The operation of the MF radar to obtain atmospheric winds is discussed by *Franke and Thorsen* [1993]. For this paper the 12 individual month composite days are used which are derived from a seven year climatology. The composite days are then analyzed to give the mean and tidal components. Mean wind data can generally be retrieved from about 60 to 100 km. Diurnal tidal data are available from 80 to 100 km, while semidiurnal tidal data can be obtained down to 60 km. However, because of averaging in amplitude and phase over each month to form the composite day, the monthly mean tidal fit may give an amplitude that is significantly smaller than the actual amplitude. This means that on any given day the actual

winds could be stronger than predicted by the climatological mean model.

The analysis for ducting or trapping uses Hickey's full wave model, as described in detail by *Hickey et al.* [1997, 1998] and by *Walterscheid et al.* [1999]. We will use the word ducted to refer to ducted or trapped waves in the remainder of the paper. The model was run for a number of conditions. The basic state winds are the MF radar winds smoothly joined to those obtained from the horizontal wind model (HWM-93) [*Hedin*, 1996] as follows: For the region 25 km below the lowest altitude of the radar data (that lowest altitude being designated $z$min), a weighted mean of the radar and HWM winds was calculated using

$$u(z) = (1 - w(z)) * \text{uhwm}(z) + w(z) * u\text{radar}(z \text{ min})$$

for $(z \text{ min} - 25 \text{ km}) < z < z\text{min}$ and where the weighting, $w(z)$, is defined as

$$w(z) = (z - z \text{ min} + 25)/25.$$

A similar procedure was applied to the joining of the winds in the 25 km region above the highest altitude of the radar data. Afterward, a smoothing spline was fit to all points to ensure that the first and second derivatives of the winds varied smoothly across the fairing regions. For both the temperature and the winds the 12 monthly composite days are averaged into six 2 month groups.

The basic state temperature data use the nighttime average lidar data smoothly joined, in a similar manner to the winds, to MSIS-90 model data [*Hedin*, 1991] for the regions above and below the lidar altitude regime. For the temperature data however, the fairing region is about 10 km. This was because the mean temperature is already smoother than the winds and is also more monotonic.

For the nominal model the wind data are then averaged over 8 hours centered at either 1200 or 2000 LT. This provides the minimum winds that might be encountered by a ducted wave. However, the model was also run for the instantaneous winds at 1600, 2000, and 2400 LT which minimizes some of the effects of averaging. Consideration of larger winds are also taken into account, as is discussed later.

3. Results

3.1. Airglow Observations

Figure 1 shows a summary of all the airglow observations from both airglow layers. They are quite similar. The data indicate that in general, based on the observed propagation directions, there were more waves originating from the south of Urbana than from the north and more from the west than from the east. There are almost no waves originating from due east or due west. The increase in wave activity in the OHM layer may be due to the greater signal levels through the OH filters used in the camera. However, because the OHM images are obtained by imaging through individual rotational lines the actual differences between the signal levels rarely differ by more than a factor of 3 and often the 02A levels are greater than the OHM levels. Thus some of the difference may indicate more waves in the OHM layer than in the 02A layer. Most of the observed waves have periods between 5 and 15 min, and typical velocities are around 50 m/s although velocities are observed as high as 80 m/s. The horizontal wavelengths are mostly between 20 and 30 km although longer wavelength
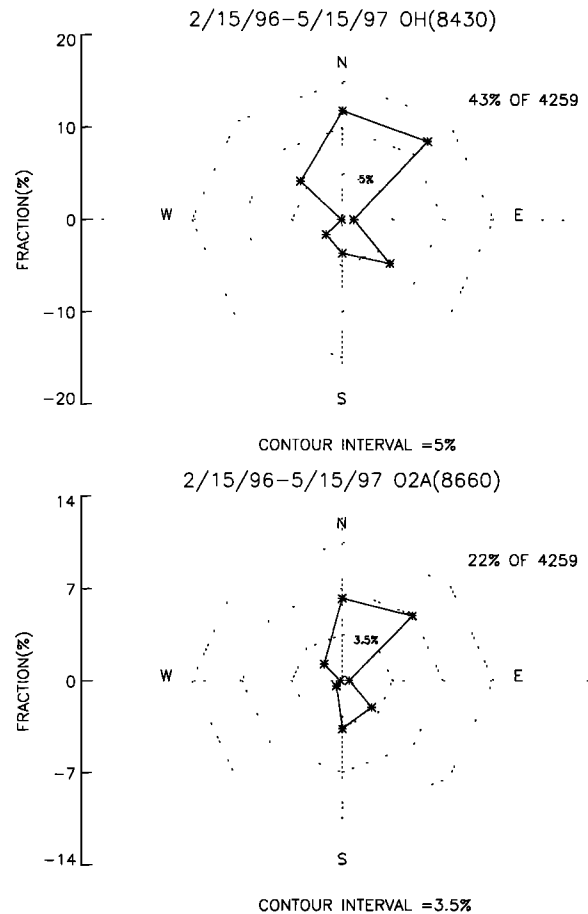

Figure 1. A summary of all the airglow observations from both airglow layers. The total number of images used and the fraction with AGWs are indicated. The plots show, as stars, the fraction of the images in which the AGWs propagated toward one of eight directions. The sum of these eight fractions is equal to the total fraction shown in the top right-hand corner. Thus the radial distance of the eight stars from the center is proportional to the wave occurrence frequency over the entire 15 month period for that direction. The top plot is for OHM emission, and the lower is for 02A emission. The contour intervals are 3.5% for 02A and 5% for OHM.

waves were observed. However, because the instrument field of view is about 90 km we are not considering here the occurrence or nonoccurrence of waves with horizontal wavelengths larger than 90 km.

Figure 2 shows the propagation directions for the 2 month periods. While there is clearly year-to-year variability, note that the largest wave activity occurs in the spring and summer periods with the peak around summer solstice. There is a distinct azimuthal anisotropy in the late spring and summer periods with waves originating from the south and southwest of Urbana. The relative frequency of waves originating from the north, as opposed to the south, becomes higher in the fall and winter periods. Waves originating from the eastern half occur frequently only in a few time periods, mainly in the fall and winter time periods. There are almost no waves originating from directly east, although in the spring, waves do appear to originate from directly west.

Recently, *Nakamura et al.* [1999] have produced a climatology of AGW observations over Shigaraki, Japan, located at
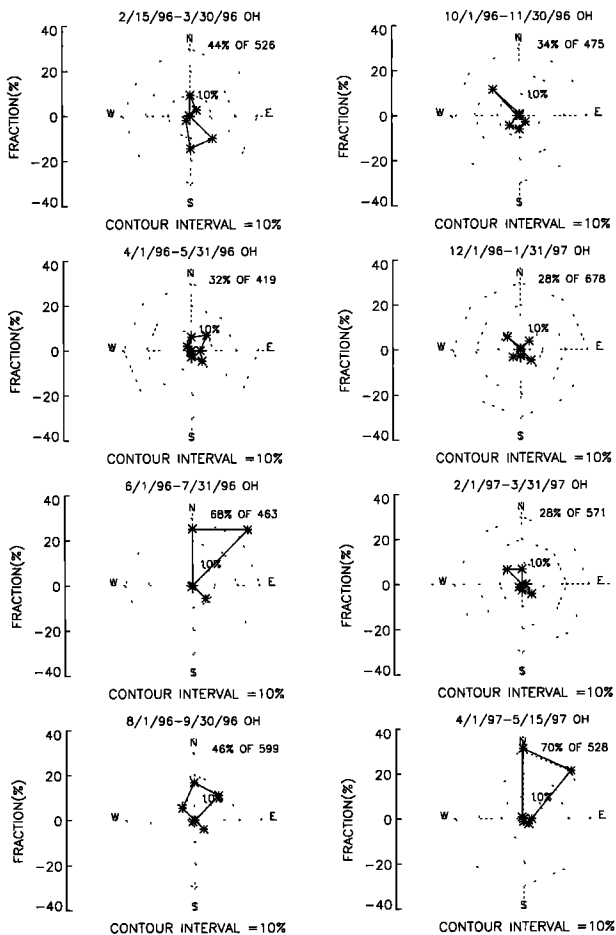
Figure 2. A summary of AGW observations for each 2 month observation period. The contour plots are the same as in Figure 1 but for OHM only.

3.2. Temperature and Wind Observations

Figure 4 shows the wind data for December/January and June/July for both the meridional and the zonal directions. The solid (dotted) line is the average of an 8 hour period centered at 2000 (1200) LT. These data show the strong mesospheric jets at around 60 km which reverse direction between summer and winter. More significant though, for the following analysis is the change in wind direction in the meridional direction between 1200 and 2000 LT during the December/January period.

Two of the plots in Figure 4 also show, as solid lines, the temperature profiles used in the modeling. For clarity in seeing the change in the mesopause height, the June/July temperature plot also repeats the December/January temperature plot shown as a heavy dashed line. The temperature climatology over Urbana is from the lidar data discussed by *States and Gardner* [2000]. The mesopause is located well above 95 km altitude in October through early March. During late March or early April the mesopause region is quite broad although the coldest temperature still occurs at a high altitude. The meso-
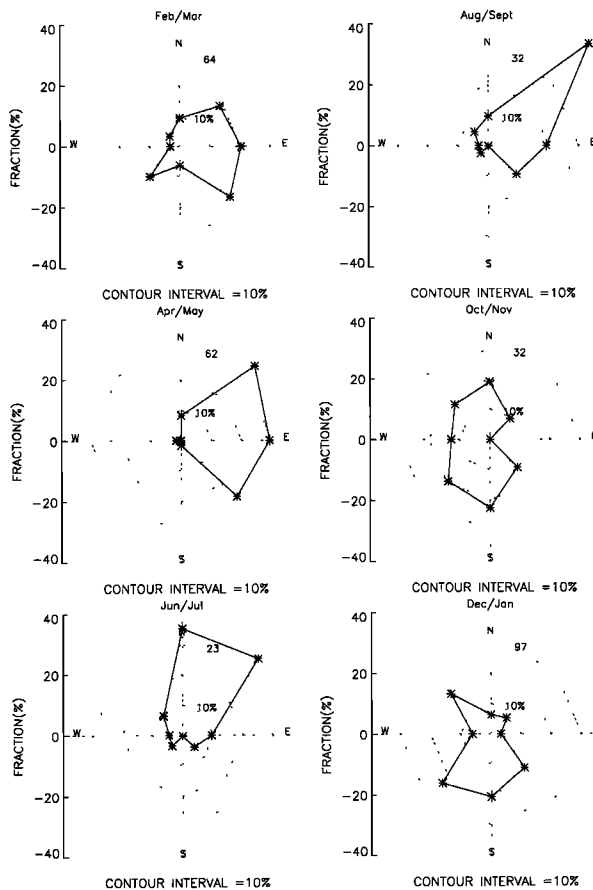

Figure 3. A summary of AGW observations taken by *Nakamura et al.* [1999] for each 2 month observation period. The contour plots are similar to Figure 2 although here six 2 month periods are taken to cover the climatology in the work of *Nakamura et al.* [1999], the first being February/March and the last being December/January. The total number of waves considered are given above each contour plot. Unlike Figures 1 and 2, each of the plots are normalized so that the eight fractions, given by the stars, total 100%. Thus the total wave occurrence frequency between the plots cannot be compared.
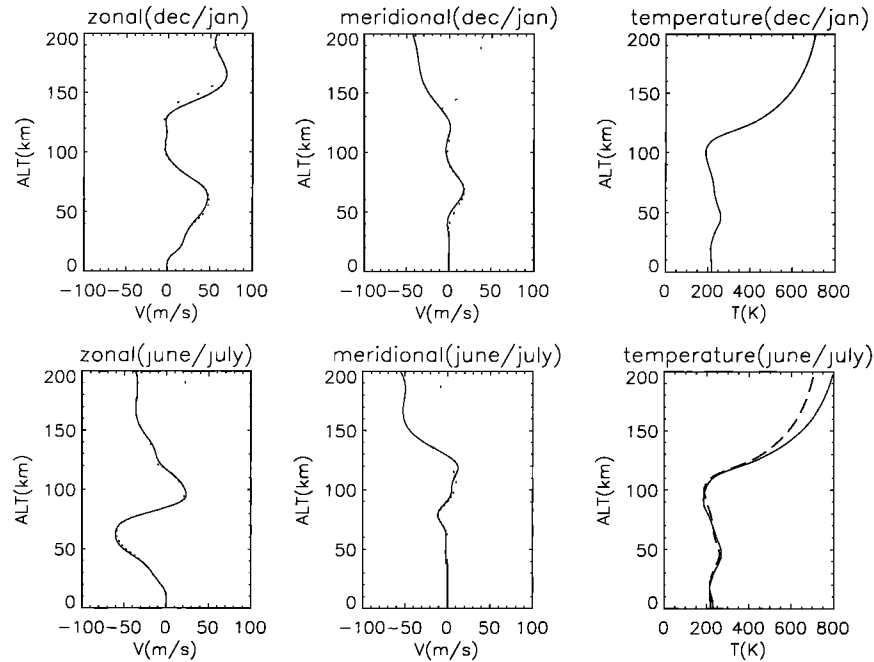
35°N. Their data were obtained over 161 nights between November 1996 and May 1998. Their climatology for AGWs of horizontal wavelength above 17.5 km shows periods mostly between 5 and 30 min with velocities mostly between 20 and 90 m/s. These numbers are comparable to what we find, although their analysis in this regard is more extensive. They have also analyzed their AGW data with respect to propagation direction. Figure 3 takes their data shown in their Figure 9 and plots it, for propagation directions over 2 month periods, in a manner similar to Figure 2 discussed above. The comparison between their observations and ours, without regard to interpretation, shows striking similarities. In April and May, most of the waves originate from the western half with many waves originating from the south and southwest. During June and July waves mainly originate from the south and southwest. In August and September there is a dominant component originating from the southwest. In October and November, most of the waves originate from the eastern half with a significant component from the northern half. In December and January the waves' origin is somewhat more symmetric than at other times, although there are fewer waves from pure east or pure west. The implications of these similarities will be discussed later.

Figure 4. Plots of the mean wind and temperature data for the December/January and June/July periods. The mean winds are averaged over 8 hours for December/January and June/July for both the meridional and the zonal directions. For the wind data the solid line is the data centered over 2000 LT, while the dotted line data are centered over 1200 LT. North and east are taken as positive for the meridional and zonal directions. For the temperature data the solid lines utilize the average nighttime data from *States and Gardner* [2000] and other model data described in the text. For comparison with the June/July temperature data, the December/January temperature data are also shown in the June/July temperature panel as a thick dashed line.

pause descends some time in late April and early May. It stays low in altitude (below 90 km) until August, and again there is a transition period in September during which time the mesopause region is broad, although the 95 km region is actually colder than the 85 km region. Note that the period of the low cold mesopause corresponds to the periods where the peak wave activity occurs as shown in Figure 2.

These wind data are averages as noted earlier and therefore their use in modeling minimizes the chance that waves may encounter critical levels or large evanescent regions. Thus Figure 5 shows the instantaneous winds at 1600, 2000, and 2400 LT. We also consider the possible effects of the large lower thermospheric winds which have been often reported [*Rosenberg*, 1968] and which may be a common and pervasive feature in the region from 100 to 130 km [*Larsen*, 2000a, 2000b].

3.3. Full Wave Model Analysis

3.3.1. Background. Two sets of results of the full wave model are discussed in the next few sections. One set is the various results for the vertical wavenumber m, which is plotted for convenience as m^2. The amplitude of an AGW at an altitude of z above a reference altitude z_0 is proportional to $Ae^{(im + 1/(2H))z}$, where A is the amplitude of the AGW at the reference altitude z_0, and H is the atmospheric scale height. If m^2 is > 0, the AGWs are freely propagating. When m^2 is 1. $\times$ 10^{-7} m^{-2}, the vertical wavelength λ_z is 20 km. Since the nominal thickness of the OH layer is 8 km, such a wave can easily be seen in airglow images. However, when m^2 is 1. $\times$ 10^{-6} m^{-2}, λ_z is near 6 km and such waves may suffer cancellation effects and not be seen in the image data. As m^2 increases above this value, the vertical wavelength continues to decrease and viscous dissi-

pation effects can become important. When viscous dissipation occurs, the efficiency of any ducting will greatly decrease. At dissipationless critical layers, m^2 becomes infinite.

If m^2 is less than zero the energy density decreases with altitude in an evanescent region. For guidance in interpreting the results of the analysis, note that when m^2 is equal to -1. $\times$ 10^{-8} m^{-2} over a 10 km altitude region, then the amplitude of the AGW decreases by $1/e$, compared to its free propagation amplitude. (The latter actually increases due to the $e^{z/2H}$ factor, as the wave passes through that region.) If the freely propagating region is bounded on the top and bottom by evanescent regions, then the wave may be ducted [e.g., *Pitteway and Hines*, 1965; *Friedman*, 1966; *Isler et al.* 1997; *Walterscheid et al.* 1999]. If the wave is tuned to the size of the duct (i.e., a half-integer number of λ_z fit vertically in the duct) and the evanescent regions are sufficiently thick, the wave will be a free-standing wave and travel horizontally with minimal energy loss. If the wave is not precisely tuned, it can still be trapped to a significant extent, but energy leakage will occur.

The other output is the kinetic energy density (K) which is proportional to the atmospheric density times the square of the wave amplitude. Since the atmospheric density decreases with respect to the reference altitude as $e^{-z/H}$, K is proportional to $A^2|e^{i2mz}|$. K can decrease for two reasons. If a critical layer or a region of high viscous dissipation is encountered the wave will begin to break down or dissipate. In such a case a wave will rapidly dissipate. If a region of evanescence is encountered where m is imaginary, the exponential factor will cause K to decrease in the layer. Some portion of the wave will be transmitted and some will be reflected. If the wave is between two such regions and the transmission is small, then the wave may
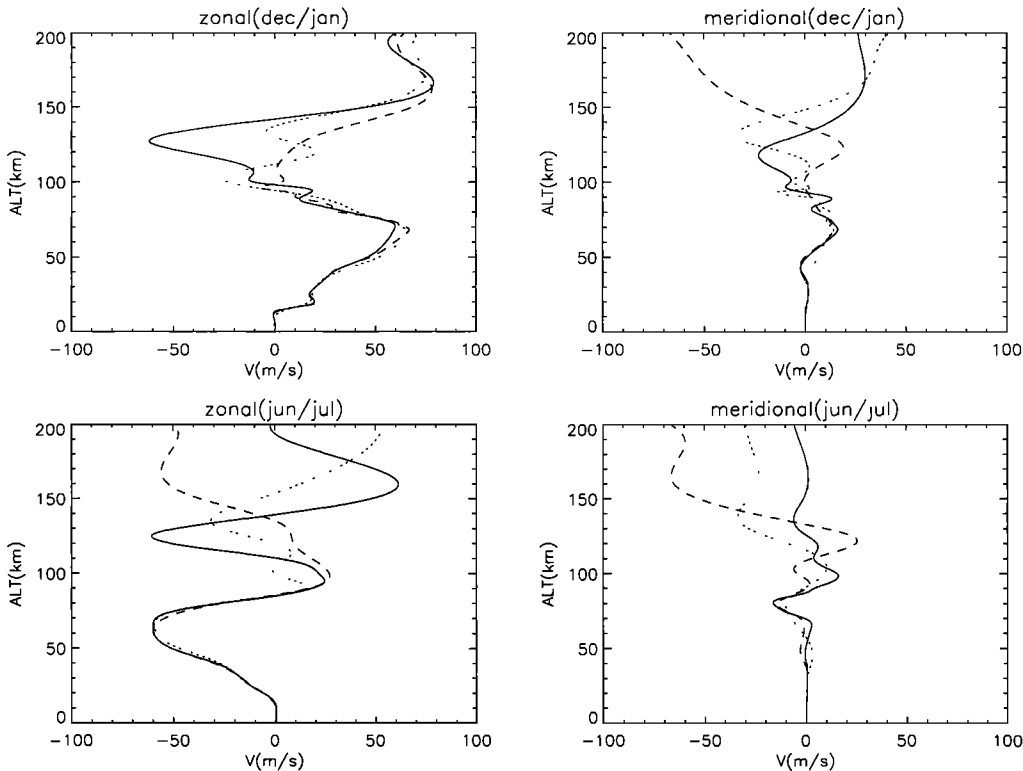
Figure 5. Plots of the wind data at three local times for December/January and June/July for both the meridional and the zonal directions. The solid line is from 2000 LT, the dotted line data are from 1600 LT, and the dashed line data are from 2400 LT. North and east are taken as positive for the meridional and zonal directions.

be efficiently ducted between the two layers without much leakage. However, since the wave has to be able to enter this propagation region, the lower region of evanescence cannot be too thick or too strong at all times and locations. For example, if the amplitude is reduced by a factor of $1/e$, then K is decreased by a factor of about $1/e^2$. We will explore this problem with a simple model described below. Again, for guidance a value of m^2 of between -0.5 and -2×10^{-8} m^{-2} over 10 km forms significant AGW trapping with the wave being able to travel considerably greater horizontal distances.

3.3.2. No wind and average wind results. First, the analysis considers using either no winds or the 8 hour average winds for either eastward, westward, northward, or southward propagating waves. The model results will be shown for only the two extreme periods: June/July, which covers the summer solstice, and December/January, which covers the winter solstice. Most of these results are for an AGW with a horizontal wavelength of 30 km and an observed period of 6 min. This is a rather fast wave (83 m/s) and is in the upper range for the observations with respect to observed phase speed. However, in this section we will also consider several other wave parameter combinations, and the next section will more thoroughly explore the dependence on phase velocity. Thus in this section the 30 km/6 min combination is used in all subsequent figures except where noted. Also, to guide the reader in subsequent m^2 figures, lines are drawn showing m^2 of zero and the 90 km altitude level.

Figure 6 shows a calculation of m^2 as a function of altitude during December/January and June/July assuming no winds. Thus this illustrates the effects of the thermal structure alone. While both periods show an upper boundary for the duct of

around 140 km, during the December/January case the evanescent region below 90 km is thin. The June/July period shows a thick (20 km) region of evanescence below 85 km with values for m^2 consistent with large vertical wavelength waves in the airglow observation region.

Figures 7 and 8 show the effect on m^2 and K, respectively, of tuning the duct for a fixed observed period. Here a wave period
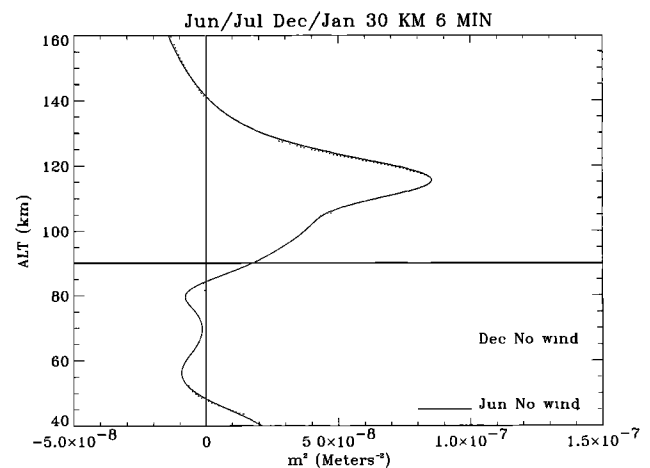

Figure 6. A plot of m^2, the square of the vertical wavenumber, as a function of altitude for two different seasons. The horizontal wavelength is 30 km, while the period is 6 min. To guide the reader in this and subsequent m^2 figures, a line is drawn showing m^2 of zero and at an altitude of 90 km.
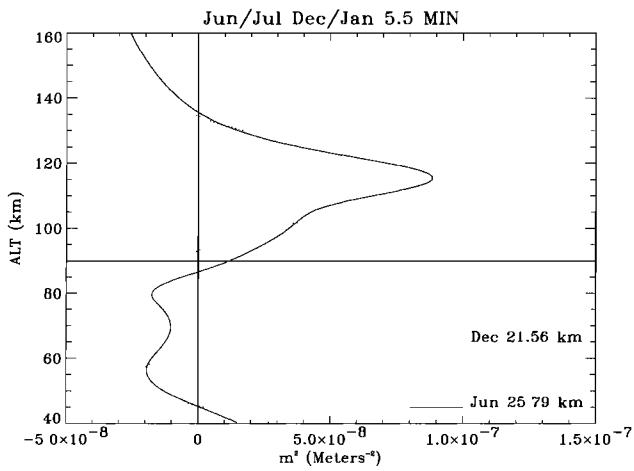
Figure 7. A plot of m^2, the square of the vertical wavenumber, as a function of altitude for a 5.5 min period wave and two different horizontal wavelengths for two different seasons.

Figure 9. A plot of the kinetic energy density of the wave as a function of altitude for three different wave periods during June/July. The horizontal wavelength is 30 km.

of 5.5 min is chosen, and two different wavelengths are shown. Both the June/July and the December/January periods are bounded by upper and lower evanescent regions. However, the lower boundary of the duct is almost 10 km higher in winter than in summer and lies above the OH emission layer region. Figure 8 clearly shows standing wave behavior indicative of strong trapping and ducting between the evanescent layers.

Figure 9 shows the effect of tuning the period on the wave ducting. This figure shows K as a function of altitude for three different wave periods during June/July. The 5.75 min period produces a standing wave that extends into the airglow region with considerable amplitude. Taken together, Figures 7–9 show that the characteristics of the duct region can greatly favor wave propagation for certain wave parameters. They are consistent with observations of quasi-monochromatic waves passing through the image region.

The above results illustrate that the thermal structure alone can produce a strong ducted region around summer solstice which would allow waves to be observed in the OH emission layer. However, the real atmosphere has winds, and these are considered in the next few figures. For the most part, only wind
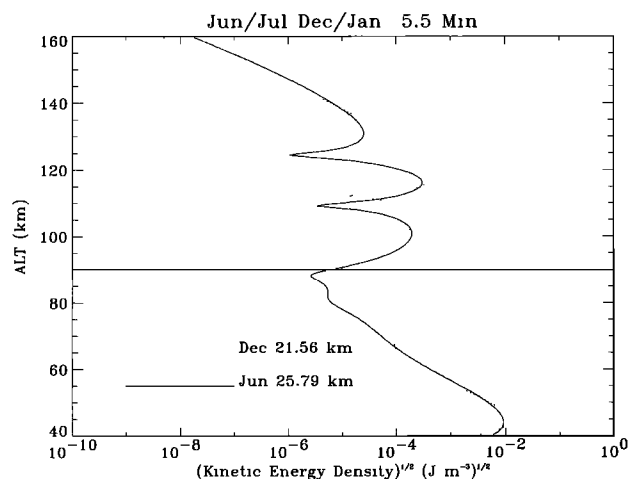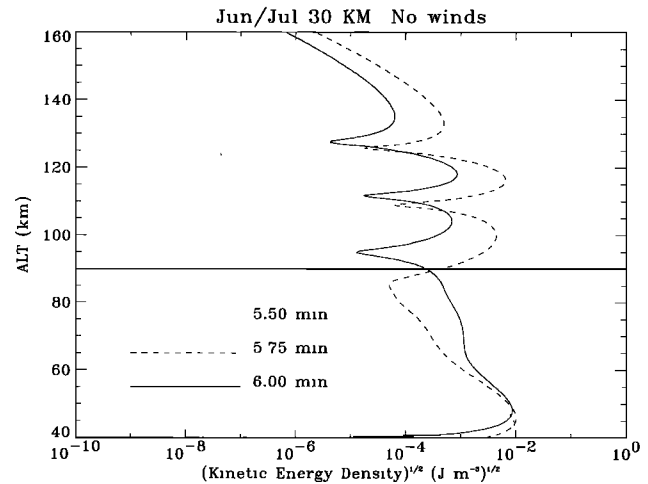
directions are considered which produce ducts (as suggested by the requirement of upper and lower evanescent regions). First are shown results for the June/July summer solstice period where the observations indicated waves propagated toward the north and northeast. The analysis for m^2, shown in Figure 10, indicates that for the modeled winds, ducting occurs for waves propagating toward the north and east. In both cases the lower boundary of the duct is within the airglow emission region. Even as the winds vary throughout the day, the duct stays stable as shown in Figure 11. However, for these winds the wave period is important. Figure 12 shows that for an 8 min, 30 km wave, traveling at 63 m/s toward the north, ducting does not occur because there is no lower evanescent region. However, only a modest increase in background winds, due to tides or gravity waves, could cause such a wave to be evanescent at or below 80 km and thus become ducted. The next section will explore this more thoroughly. Results for December/January indicate that ducting is somewhat more difficult for this period.

Figure 8. A plot of the kinetic energy density of the wave as a function of altitude for the waves considered in Figure 7.
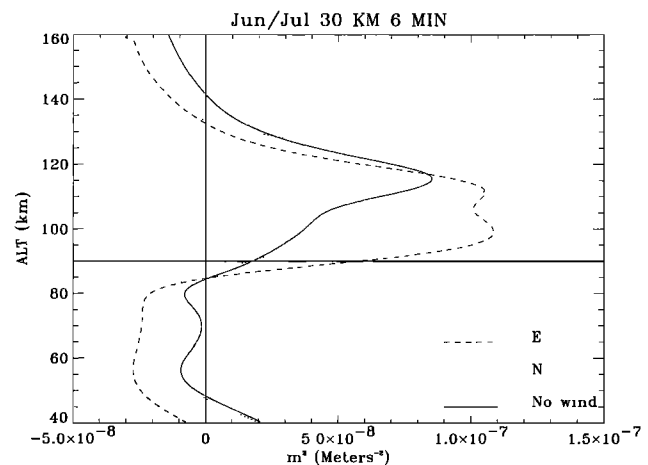

Figure 10. A plot of m^2, the square of the vertical wavenumber, as a function of altitude for a 6 min period, 30 km horizontal wavelength wave for three cases of wave propagation. Arbitrary direction (no wind), northward wave, and eastward wave. All for June/July.
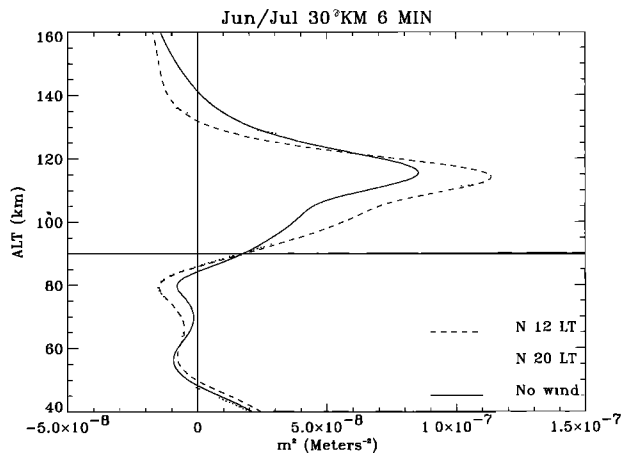
Figure 11. Same as Figure 10 except the eastward wave is replaced by a northward wave with the background winds averaged at 1200 LT.

Figure 13. Same as Figure 10 except for December/January and the two waves are southward and westward.

Figure 13 shows that westward waves can be ducted, while southward waves would not because of the absence of an upper boundary to the duct.

In the previous analysis it has been indicated that eastward waves in the summer and westward waves in the winter can be ducted. However, as Figure 14 illustrates, there is a large decrease in K between the assumed source of the waves (below 40 km altitude) and the ducted region above 80 km. Thus as will be argued below, it is unlikely that such waves would be observed. Modeling was also performed for other seasons, and as expected, there is considerable increase in the K in the ducted region for waves traveling eastward in early spring and westward in early fall associated with the diminished eastward and westward jets around equinox.

Taken together this simple analysis suggests that the most likely waves to be ducted and observed are those propagating toward the north, and thus originating from the south, in the summer solstice period consistent with observations. However, waves originating from the west would lose too much energy while traversing the evanescent region below 80 km. Waves originating from the southwest, however, may find the lower evanescent region thin enough to enter the duct without significant loss of energy, yet thick enough to facilitate significant
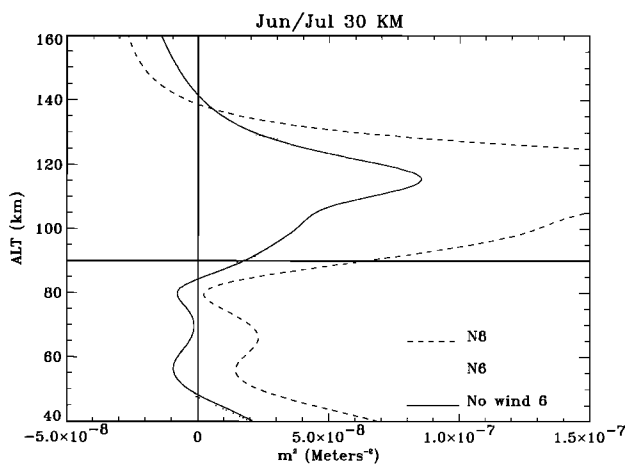
ducting and to allow reasonable propagation distances. In addition, the analysis was performed for fast waves (83 m/s). Next we explore the sensitivity of the dueling to wave velocity and direction.

3.3.3. Instantaneous winds and three wave velocities. The use of average winds minimizes the effects of wind peaks that can increase or decrease the evanescent regions or even cause the appearance of critical layers. Thus in this section, we investigate the use of instantaneous winds for 1600, 2000, and 2400 LT. The meridional and zonal winds for these times are shown in Figure 5. Three different wave combinations are taken: the 6 min, 30 km (83 m/s) wave discussed above, one traveling at 52 m/s with a period of 8 min and a horizontal wavelength of 25 km, and a slow wave traveling at 33 m/s with a period of 10 min and a horizontal wavelength of 20 km. These parameters cover the velocity regime of the observations. Since waves were sorted according to propagation direction using octants, each covering 45°, four directions are considered here: north and northeast propagation in June/July and south and southwest in December and January.

Each of the following four figures has six plots, three of K

Figure 12. Same as Figure 10 except the eastward wave is replaced by a northward wind with a period of 8 min.

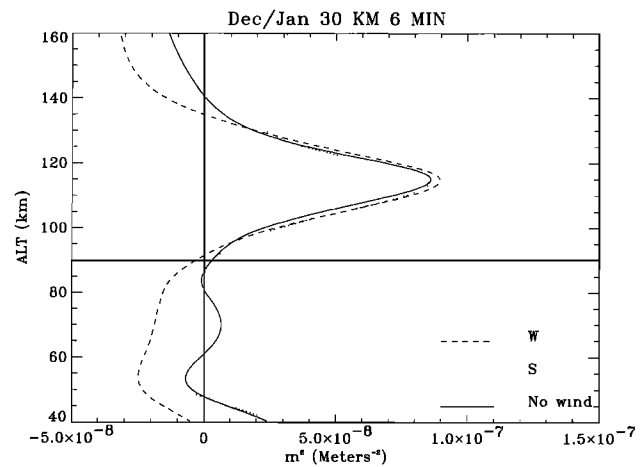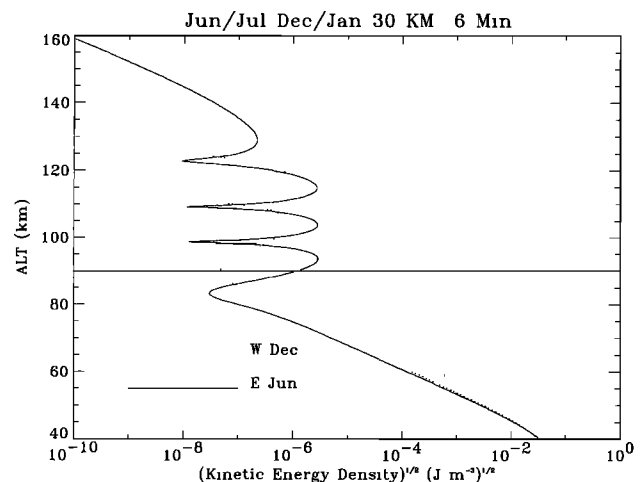**Figure 14.** Plots of the kinetic energy density for two cases. An eastward wave in June/July and a westward wave in December/January.
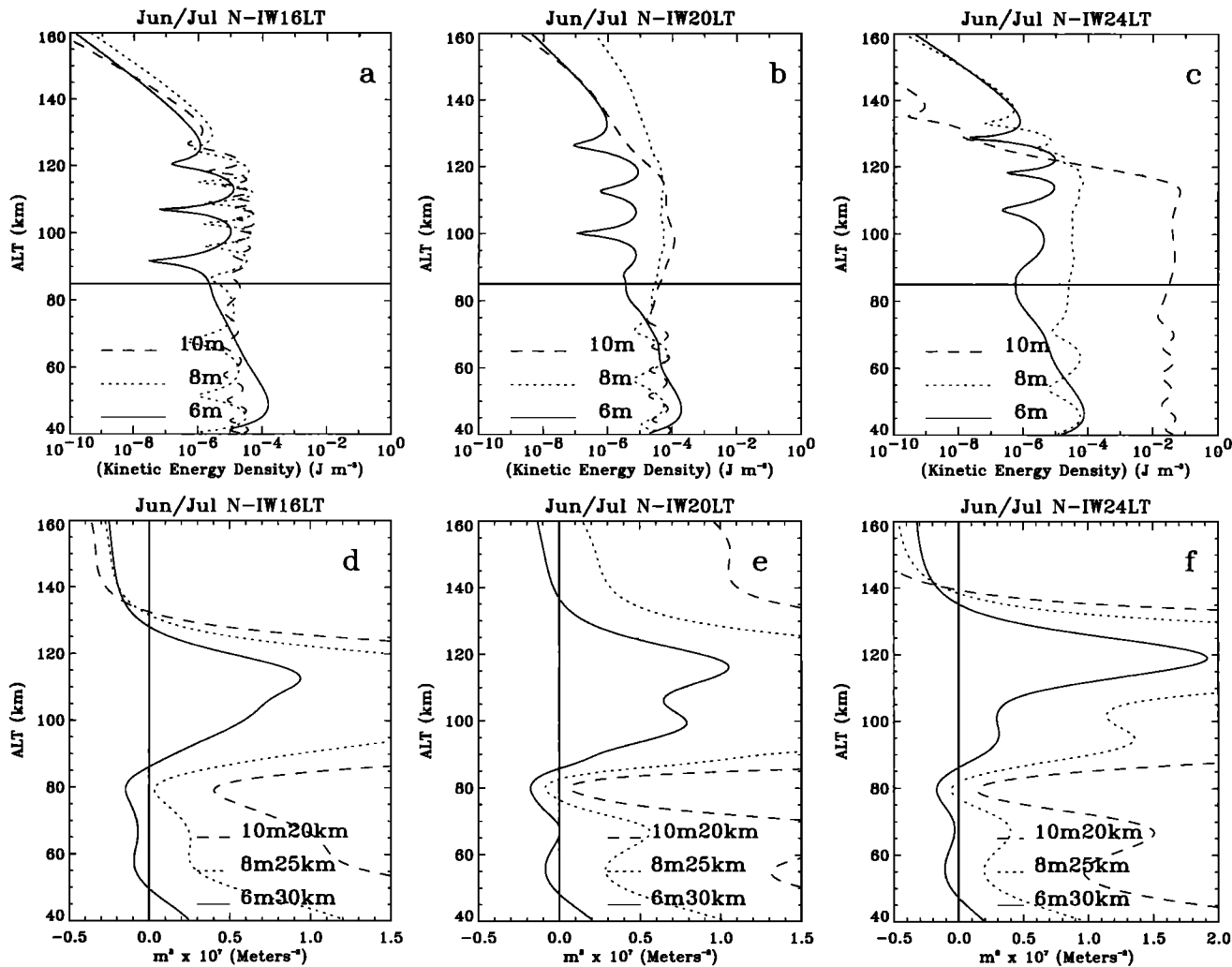
Figure 15. All are for northward propagating waves of one of the three combinations of observed period and horizontal wavelength: 6 min, 30 km; 8 min, 25 km; or 10 min, 20 km. Six panels are divided between plots of m^2 versus altitude and K versus altitude. The winds are the instantaneous winds at either 1600, 2000, or 2400 LT. (a) K at 1600 LT, (b) K at 2000 LT, (c) K at 2400 LT, (d) m^2 at 1600 LT, (e) m^2 at 2000 LT, (f) m^2 at 2400 LT.

and three of m^2, at 1600, 2000, and 2400 LT. On each plot the solid line is the 6 min, 30 km (83 m/s) wave, the dotted line is the 8 min, 25 km (52 m/s) wave, and the dashed line is the 10 min, 20 km (33 m/s) wave. Figure 15 shows results for waves propagating toward the north during the June/July period. While the fast 6 min wave has upper and lower evanescent regions at all times, this is not generally true for the other waves. Thus in the K plots, only the fast wave shows evidence of ducting behavior, with K decreasing between altitudes of 50 and 80 km, then showing oscillatory behavior at higher altitudes consistent with a ducted wave, and then decreasing again above about 130 km. Interestingly, K for the slow 10 min wave shows a large decrease (Figure 15c) above 120 km even though m^2 is positive (Figure 15f). This is because m^2 is large (the vertical wavelength is small), and the wave is losing energy due to viscous dissipation. This is an example of the wave energy not being ducted but rather being lost to the background atmosphere.

Figures 15 and 16 show, however, that a small change in propagation direction can cause ducting of even the slower

waves. At 1600 and 2400 LT there are upper and lower evanescent regions for all three waves. This shows that the ducting of these waves is quite sensitive to propagation direction. For June/July it would be expected therefore that ducted waves would propagate somewhere between north and northeast depending on the characteristics of the wave and the exact background wind. This will be explored further in section 4 of the paper. The K plots also indicate that although evanescent regions favorable to ducting exist for all three wave periods, the winds are such that only around 1600 LT would the 10 min waves be ducted. At 2400 LT these slower waves lose energy due to viscous dissipation. Also, for these modeled winds the time period around 2000 LT would be less favorable for wave ducting. The upper portion of the duct would be leaky. This shows that modification of the winds by variable tides or large-scale AGWs could have an important effect on whether ducting could proceed during these time periods.

Figures 17 and 18 show the comparable results for south and southwest propagating waves during December and January. There are certainly time periods where conditions favorable
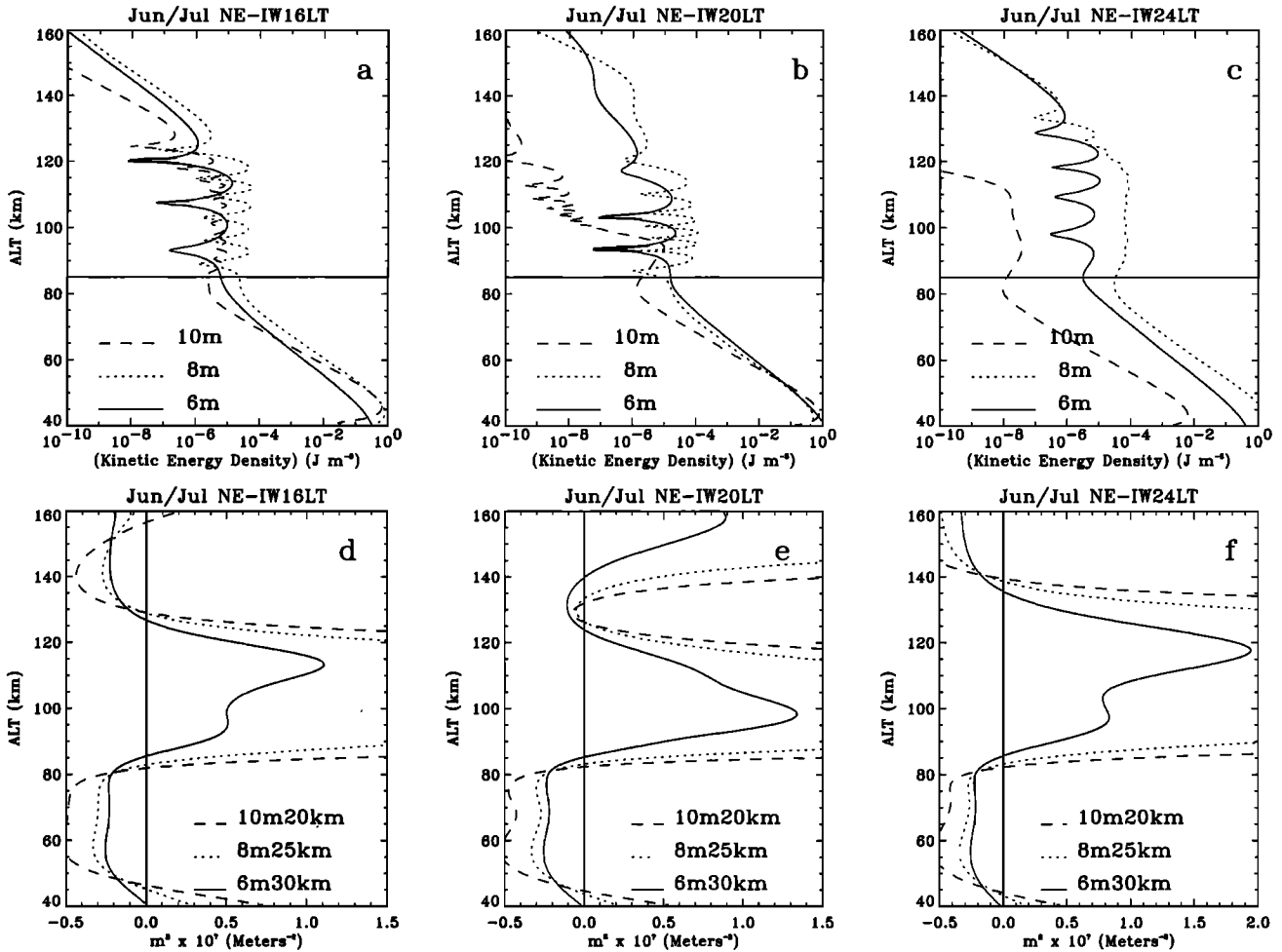
Figure 16. Same as Figure 15 but for northeastward propagating waves.

4. Discussion

4.1. A Simple Model for the Ducted Region

for ducting should occur, although as noted earlier, the ducting region is a few km higher than around June/July. The ducting, however, is not quite so favorable, even for the faster waves, as it is around summer solstice.

The characteristics of the evanescent regions must be in a certain range in order to overcome the following problems: If the evanescent region at the bottom of the duct is thick (so that mz, the product of the vertical wavenumber and the thickness of the evanescent region is much greater than 1), AGWs will lose a significant portion of their energy in tunneling through and entering the ducting region. At that point, however, the duct is almost lossless, and the AGW can propagate horizontally a great distance without losing significant energy. If, however, mz is small and the AGW loses little energy on passing through the evanescent region, then the duct will be quite lossy and the wave can propagate only a short distance. However, this means that the actual wave parameters (period, horizontal wavelength) of the ducted wave may be somewhat different than the cases chosen for this study, as illustrated above in Figure 7.

A simple model can reveal an estimate of what the wave amplitude will look like after traveling a given distance. Here we use a three layer region model similar to that shown in Figure 19. The bottom and top layers allow a freely propagating wave of vertical wavenumber m_p. The middle layer of thickness z is evanescent with m^2 less than 0. A wave of unity amplitude is incident from the bottom layer and there is a reflected wave of amplitude B in this layer. In the evanescent region there are waves of vertically increasing and decreasing amplitudes C and D, respectively. In the top layer there is an upward energy propagating wave of amplitude E. The boundary conditions at each interface follow those from *Walterscheid et al.* [1999]; the wave vertical velocity and its derivative are continuous. The fraction of the incident kinetic energy density which are reflected and transmitted in the two freely propagating regions are given by B^2 and E^2 which can easily be obtained. If there is an additional identical evanescent region above, then these solutions can be used to estimate the amplitude of the AGW after it has reflected N times between the two layers. A schematic of such a trapped wave is shown in Figure 20. The fraction of the incident kinetic energy density of the wave passing through the lower evanescent region is given by E^2. Then after every reflection the reflected energy is reduced by a factor B^2. The resultant wave amplitude after N reflections is $E(B)^N$. Table 1 gives the results of varying m for various fixed values of N, and a constant thickness of 25 km for z, to find the maximum wave amplitude, Amp(N) after N bounces. The 25 km value was used because this is a typical
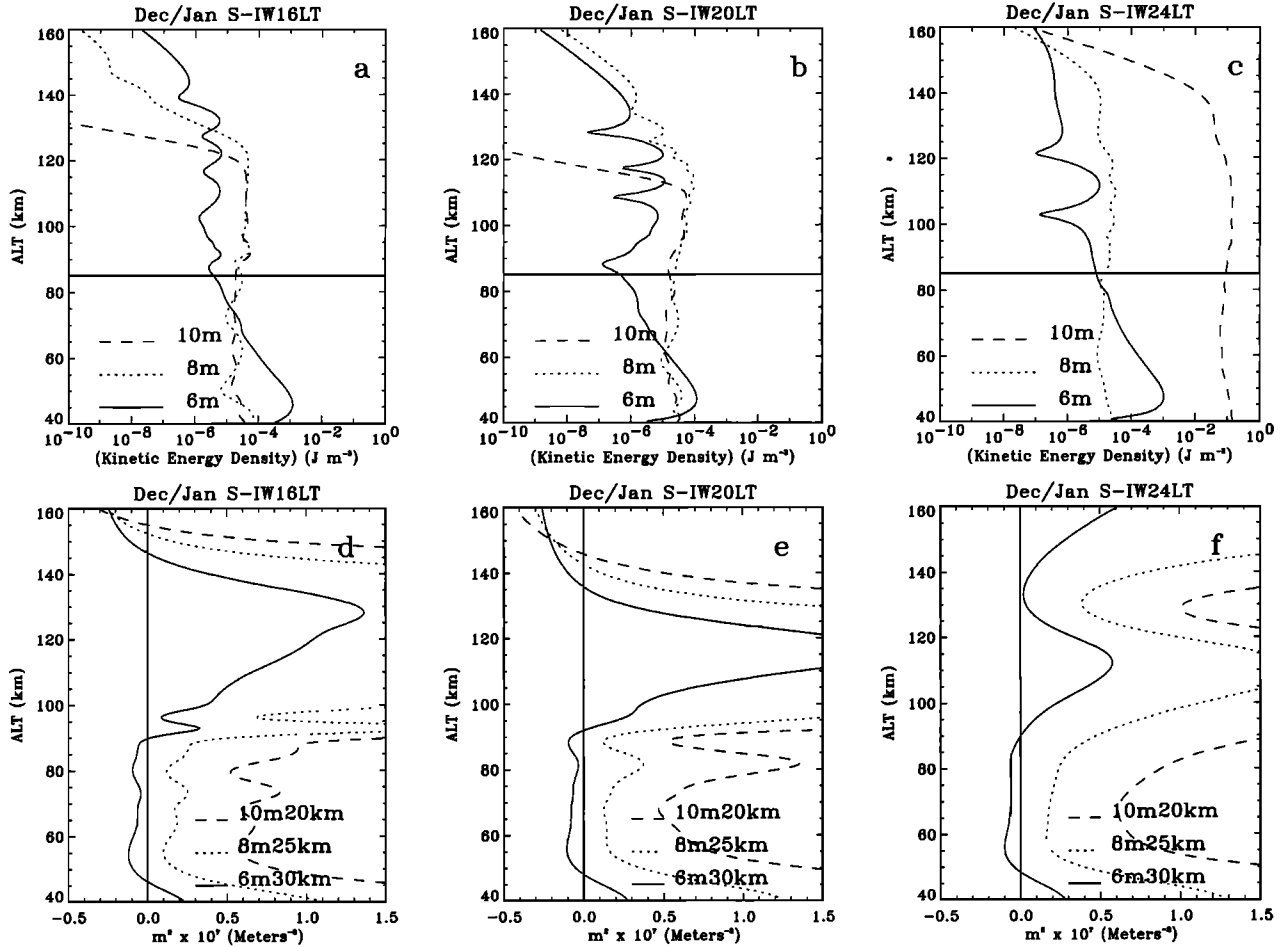
Figure 17. Same as Figure 15 but for southward propagating waves.

thickness of the lower evanescent region. Note that after the initial entry into the ducted region the amplitude is $A(0)$, and $A(N)$ is about 40% less than $A(0)$. In these calculations, m_p^2 is taken as 10^{-7} m^{-2}, and thus the vertical wavelength in the free propagating region is 20 km.

These results allow an estimate of how far a ducted AGW packet of period τ, vertical wavelength L_z, and vertical group velocity w_g, can travel. For example, if the propagation region is D km thick, the AGW will encounter a reflection every D/w_g periods. The vertical and horizontal phase velocities are within about a factor of 2 of their respective group velocities for the waves considered here. The group velocities are always less than the phase velocities. Thus for the waves considered here, w_g is taken as $\sim L_z/\tau$, and a reflection occurs every D_τ/L_z period. If, for example, D is 40 km and L_z is 20 km, the AGW packet will encounter a reflection after two periods. Thus for each bounce the AGW travels 50 km horizontally if the horizontal wavelength is 25 km. If we assume that one of the evanescent regions is very thick and no loss occurs at that boundary, then the AGW would travel 100 km between lossy reflections. On the basis of the results presented in Table 1, after 4000 km (or 40 lossy bounces) the amplitude is just less than 10% of the original value and K is down by a factor of 100. For this situation the optimum m^2, in the evanescent region, is -4.4×10^{-9} m^{-2}, which is well within the range of values for northward and northeastward propagating waves in June/July.

Tables 2 and 3 give the results for this simple model for various combinations of N bounces and mz assuming z is either 25 km (Table 2) or 15 km (Table 3). These results will be discussed next.

4.2. Wave Amplitudes and Propagation Directions

The results provided in Table 1 suggest that for ducting over reasonable distances (1000–3000 km) the wave amplitude will be about 10% of the original wave amplitude. Is this reasonable? For the waves observed over Urbana the amplitudes of the intensity waves were a few percent of the background intensity. (The signal to noise of the images is about 100 to 1, so percentage fluctuations below about 1% would not be observable.) The equivalent temperature or density fluctuations may be inferred from Krassovsky's eta, which is the ratio of the airglow intensity and temperature fluctuations. For OHM emissions this value is probably above 6, while for 02A it is slightly less, being around 5 for the period and wavelength of the waves considered here [*Schubert et al.*, 1991; *Hickey et al.*, 1993]. Thus the measured AGW temperature or density amplitudes are about 0.5% of the background. Measured amplitudes of a few tenths of percent are consistent with wave amplitudes incident on the duct of a few percent, which seems reasonable. Indeed, typical AGW relative density amplitudes are 5% as measured by *Senft and Gardner* [1991] with a Na lidar over Urbana. Perhaps, more relevant data are those of *Gardner and Voelz* [1987] who measured the seasonal characteristics of monochromatic waves seen over Urbana using a Na
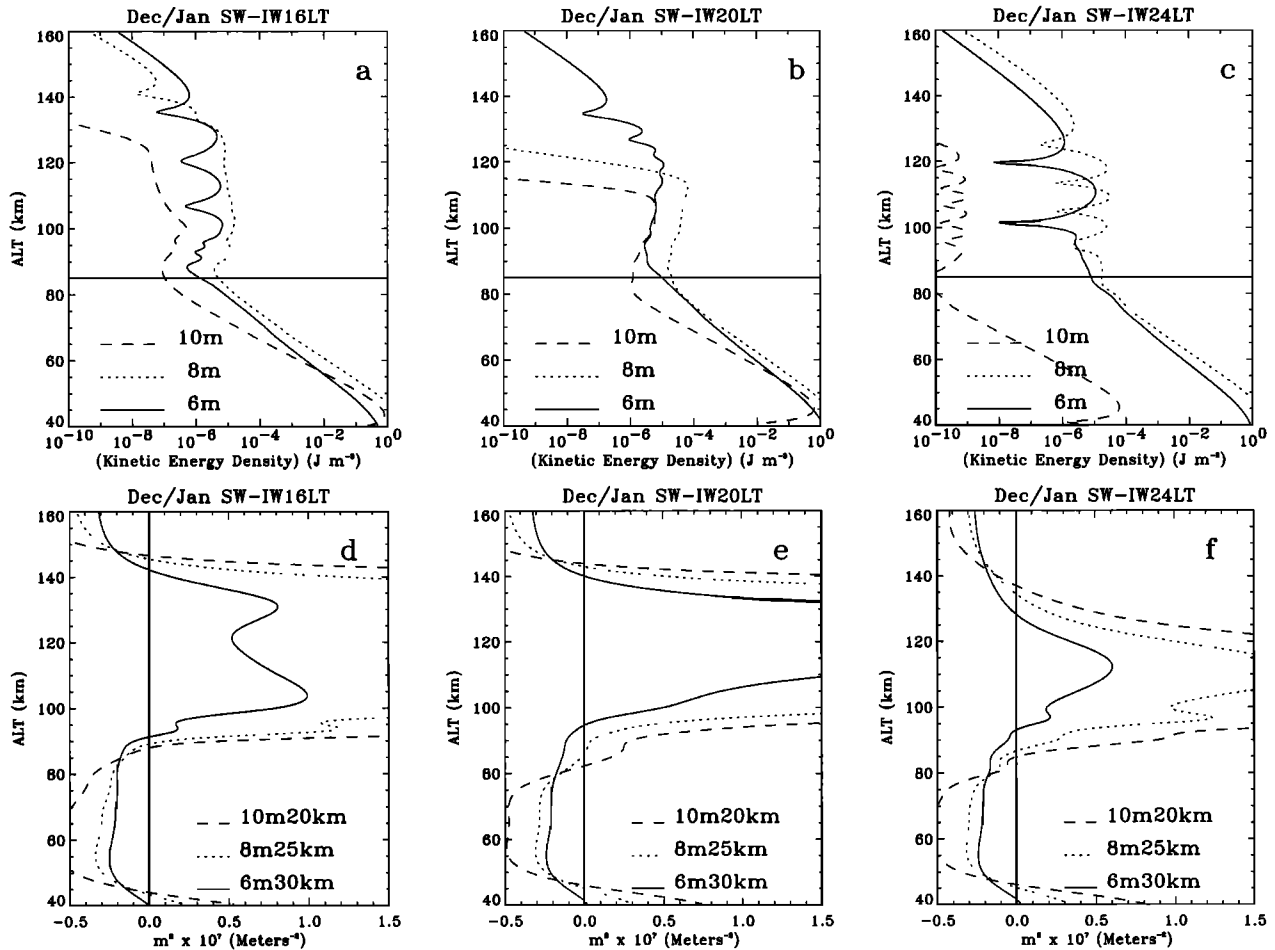
Figure 18. Same as Figure 15 but for southwestward propagating waves.

lidar. For waves with a minimum period of 25 min they found relative fluctuations of a few percent at 90 km. On the basis of the results presented earlier, such large-period waves probably were not ducted. These data suggest that small-scale waves may have nominal amplitudes at 90 km of a few percent, and thus a 10% reduction to a few tenths of percent would be close
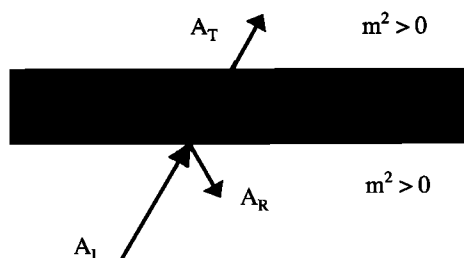

Figure 19. A schematic representation of a freely propagating wave A_I incident on an evanescent region where the vertical wavenumber m becomes imaginary. A wave designated A_R is reflected at the boundary, while a wave designated A_T is transmitted through the evanescent region into an upper freely propagating region. In both freely propagating regions the vertical wavenumber is real. The dashed line in the evanescent region indicates that the wave is not freely propagating in that region. The evanescent region is shaded.
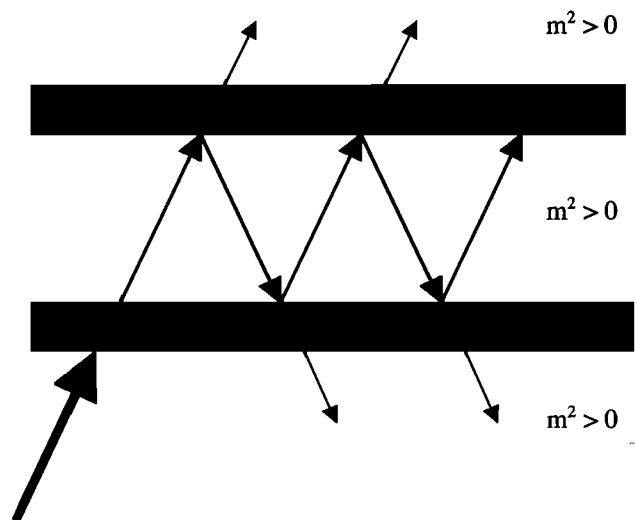
Figure 20. Similar to Figure 19 this shows a schematic representation of a freely propagating wave trapped between two evanescent regions where the vertical wavenumber m becomes imaginary. The trapped wave entered from below, first passing through an evanescent region. Some of the trapped wave energy leaks out of the trapped region through the upper evanescent region. The thickness and size of the lines represents in a qualitative way the relative wave energy in the various regions.

Table 1. Max Amplitude After N Bounces

N	Amp(0)	Amp(N)	mz	m^2 ($z = 25$ km)
20	0.218	0.134	0.8	-1.1×10^{-9}
30	0.179	0.110	1.4	-3.0×10^{-9}
40	0.156	0.095	1.7	-4.4×10^{-9}
50	0.139	0.085	1.9	-5.6×10^{-9}
60	0.127	0.078	2.0	-6.6×10^{-9}
70	0.118	0.072	2.2	-7.4×10^{-9}
80	0.111	0.068	2.3	-8.1×10^{-9}
90	0.104	0.064	2.3	-8.8×10^{-9}
100	0.099	0.061	2.4	-9.4×10^{-9}

Table 3. Amp(N, mz, $z = 15$ km)

N	Amp(0)	Amp(N)	mz	m^2 ($z = 25$ km)
25	0.260	0.108	1.5	-1.0×10^{-8}
25	0.135	0.107	2.5	-2.8×10^{-8}
30	0.260	0.091	1.5	-1.0×10^{-8}
30	0.135	0.102	2.5	-2.8×10^{-8}
35	0.260	0.076	1.5	-1.0×10^{-8}
35	0.135	0.098	2.5	-2.8×10^{-8}
40	0.260	0.064	1.5	-1.0×10^{-8}
40	0.135	0.093	2.5	-2.8×10^{-8}
45	0.260	0.054	1.5	-1.0×10^{-8}
45	0.135	0.089	2.5	-2.8×10^{-8}

to what we observed. Also, given the signal to noise of the Urbana airglow instrument, waves whose amplitudes are below 5% would be difficult to observe.

Table 1 shows that the optimum values for m^2 are around $-5. \times 10^{-9}$ m^{-2}. Comparison with Figures 15–18 suggests that given these values, the optimum directions are between northward and northeastward in June/July and between southward and southwestward in December and January.

Note that for eastward wave propagation in June/July, almost no waves are seen in the Urbana data. The mz for this case is around 4, and the values for m^2, in the evanescent region, are around -3×10^{-8} m^{-2}. From Table 2 such values would result in a wave amplitude of around 3% due to passage through the mesospheric wind jet region between 50 and 80 km. Calculations also show for the regions where m^2 is even more negative, the amplitude would be around 1% of the original value. Thus the absence of eastward propagating waves over Urbana may be partially a limitation of the instrument. The Japanese data reported on by *Nakamura et al.* [1999] should have several times the signal to noise since those observations are of multiple OHM bands whose total intensity is over an order of magnitude brighter than the rotational line used in the Aerospace instrument. Thus eastward propagating waves, if ducted, should be more easily seen and indeed Figure 3 shows the presence of such waves.

4.3. Variations in Lower Thermospheric Winds and the Timescale for Ducting

The analysis in this paper uses climatological winds. Even with these average winds there are periods when ducting is weak, as seen in Figure 16. Thus the timescale over which ducting is effective may be much less than a semidiurnal tidal period. Such tides are responsible for much of the variation

Table 2. Amp(N, mz, $z = 25$ km)

N	Amp(0)	Amp(N)	mz	m^2 ($z = 25$ km)
15	0.207	0.149	1.0	-1.6×10^{-9}
15	0.169	0.136	1.5	-3.6×10^{-9}
15	0.130	0.114	2.0	-6.4×10^{-9}
15	0.029	0.029	4.0	-2.6×10^{-8}
35	0.207	0.096	1.0	-1.6×10^{-9}
35	0.169	0.102	1.5	-3.6×10^{-9}
35	0.130	0.096	2.0	-6.4×10^{-9}
35	0.029	0.029	4.0	-2.6×10^{-8}
55	0.207	0.062	1.0	-1.6×10^{-9}
55	0.169	0.076	1.5	-3.6×10^{-9}
55	0.130	0.081	2.0	-6.4×10^{-9}
55	0.029	0.029	4.0	-2.6×10^{-8}

above 100 km. If waves travel at nominally 50 m/s, then this suggests waves originate from distances only a few thousand kilometers at most from the observation site. The background tidal winds are highly variable though, and in some cases, these variations may also reinforce the ducting of the waves, allowing an increase in propagation distance.

However, recent work by *Larsen* [2000a, 2000b] suggests that there are frequently quite large winds, often exceeding 100 m/s, within the 90–120 km region. These winds, which are not included in models, are long-lived and may appear to be wave-like with periods close to 12 hours. Depending on the phase and direction, such winds could form the upper evanescent region necessary for ducting. This possibility is explored by noting that the thickness of the regions where the waves exceed 50 m/s, or in some cases approach 100 m/s, can be as large as 15 km, based on the few examples shown by *Larsen* [2000a, 2000b]. Winds of those magnitudes can produce values for m^2 of almost $-3. \times 10^{-9}$ m^{-2}. Table 3 shows calculations made for such a ducted region. By comparing Amp(N) to Amp(0), it is apparent that the reduction in amplitude in bouncing off such an upper boundary layer is the same as when a bounce is made off the lower boundary layer at 80 km. Thus the presence of such winds would not preclude a ducted region. However, if the winds are in the opposite direction, a critical layer would be encountered instead of an evanescent region. Thus for wave periods of around 12 hours the period where the evanescent region is encountered may be only 6 hours or so. Therefore the horizontal propagation distance may be less than 1500 km when such winds are present. In addition, their occurrence down to 95 km might even explain the relative absence of waves in the O2A layer.

4.4. Implications for the Observations

The analysis supports the seasonality of the observations that waves are seen from specific directions at certain times of the year. As *Walterscheid et al.* [1999] found, this analysis shows that the ducted region is generally lower around summer solstice than around winter solstice due to the change in mesopause height. This means that the OHM airglow region is more likely to be in the duct in the summer solstice period consistent with the greater observation of AGWs during this period. The model also predicts that waves propagating toward certain directions should be more easily ducted than waves propagating toward other directions. In particular, there is a large increase in wave activity observed originating from the south and southwest of Urbana during the spring and summer periods. Such strong azimuthal anisotropy was also evident in the Japanese data set even though their observations are more

sensitive than the Urbana data. The Japanese data show relatively fewer waves propagating eastward compared to those that propagate north and northeastward during June/July. The strong azimuthal anistropy around summer solstice was also found at Adelaide, and as *Walterscheid et al.* [1999] argued, those observations can be explained by both the presence of ducting and the strong sources from well equatorward of Adelaide during this period.

For the Urbana data the strong sources are probably associated with the intense convective activity that occurs over Texas and the Gulf of Mexico in the spring and summer. Such activity is also present south of Japan in the summer [*Tai and Ogura*, 1987]. Recent data from the Lightning Imaging Sensor on the Tropical Rainfall Measuring Mission (TRMM) satellite also show a large increase in lightning south and southwest of Japan, as well as in the southern United States in the spring and summer compared to the fall and winter [*Christian et al.*, 1999; D. Buechler, 2000, private communication; http://thunder.nsstc.nasa.gov/data/query/distributions.html]. Lightning should be a proxy for convective activity [D. Buechler, private communication, 2000; *Goodman et al.*, 1988] Indeed, a recent study by *McLandress et al.* [2000] does suggest that gravity wave activity in the summertime in the stratosphere is associated with the strong convective activity in the Great Plains area of North America and southwest of Japan.

However, waves originating locally, as produced by late afternoon thunderstorms near Urbana, probably will have passed through the airglow emission layer before observations even begin. Such waves also would show no pronounced azimuthal anistropy since convective activity is likely to be isotropically distributed around Urbana. This is a plausible argument for ducted waves originating a considerable distance from Urbana. Moreover, the wave images show that these waves appear to move coherently from one side of the image to the other. If the waves were not ducted, the waves should be seen in an airglow layer for nominally one cycle before passing through the layer.

In the winter, AGWs could be ducted under certain conditions as they travel south and southwest. The arguments above suggest that ducting would be more lossy during the winter because of the high mesopause, and thus there should be less north-south asymmetry in winter than in summer. The strong azimuthal anisotropy seen around the summer solstice is indeed absent in the Urbana data. This could, however, also be explained as the result of a selection process because the *Nakamura et al.* [1999] data do show an increase in wave propagation toward the south in winter. However, in those data the asymmetry is less than in summer. Moreover, the observations do not appear to show a bias for waves propagating southwest as the model analysis predicts. This suggests less ducting during the winter.

Finally, the relative lack of observations of AGWs from due east or west seems consistent with the analysis that shows that such ducted waves would be severely attenuated in the lower evanescent region before entering the duct. Given the plausible wave sources, AGWs originating from those directions could occur during the short periods where the mesospheric jet reverses. This would occur in April, when the mesopause has begun to descend in altitude and, in fact, this is the one period where such waves were seen in some numbers in the Urbana data. More such observations are needed however.

5. Conclusions

The main conclusions of this paper are as follows:

1. New observations reported here show that in the spring and summer, and especially around summer solstice, most of the observed AGWs propagate toward the north or northeast of Urbana. Similar climatological observations from Japan also show similar propagation directions, with respect to the observation site, for those AGWs. Observations from other periods in the fall and winter do not show such strong directionality although there is a bias in both data sets for wave propagation toward the eastern half as opposed to the western half of the sky with respect to both observation sites. In both observation sites however, AGWs less frequently propagate due east or west.

2. A full-wave model analysis, using measured lidar temperatures, indicates that in the absence of winds the temperature structure around the mesopause would suggest that waves may be ducted. The region of free propagation is somewhat lower around summer solstice than around winter solstice. This is similar to what was previously found for the Adelaide, Australia, region.

3. When winds are included in the model, waves would be ducted if they originate, with respect to the observation site, from the south and southwest around summer solstice and from the north and northeast around winter solstice. The model analysis indicates that the ducting may be quite sensitive to the exact wave direction.

4. The period of the ducted waves is between 5 and 10 min with horizontal wavelengths of from 20 to 30 km.

5. The absence of strong wave activity originating from the north and northeast in the winter as well as the very strong wave activity originating from the south and southwest in spring and summer must also be a consequence of wave sources. Strong convective activity is present during the spring and summer but is less frequent during the fall and winter.

6. A simple model was constructed to estimate the propagation distances for ducted waves. The model indicates that such waves may originate no more than a few thousand kilometers from the observation site. The amplitudes of these waves is about 10% of the original amplitude. Waves originating from the east around summer solstice would have amplitudes about 1% of the original amplitude. The absence of such waves in the Urbana data may be a selection process as they were observed in the more sensitive Japanese observations.

7. The model also suggests that the very large scale winds in the 95–120 km region recently reported on and discussed by Larsen do not preclude the ducting of AGWs. Such winds may form the upper evanescent region needed for the ducting of some waves.

References

Chimonas, G., and C. O. Hines, Doppler ducting of atmospheric gravity waves, *J. Geophys. Res., 91*, 1219–1230, 1986.
Christian, H. R., et al., The Lightning Imaging Sensor, Preprints, *NASA/CP-1999-209261*, pp. 746–749, 1999.
Francis, S. H., Lower atmospheric gravity wave modes and their rela-

tion to medium-scale traveling ionospheric disturbances, *J. Geophys. Res.*, *78*, 8289–8295, 1973.

Francis, S. H., Global propagation of atmospheric gravity waves: A review, *J. Atmos. Sol. Terr. Phys.*, *37*, 1011–1054, 1974.

Franke, S. J., and D. Thorsen, Mean winds and tides in the middle atmosphere at Urbana (40°N, 88°W) during 1991–1992, *J. Geophys. Res.*, *98*, 18,607–18,615, 1993.

Friedman, J. P., Propagation of internal gravity waves in a thermally stratified atmosphere, *J. Geophys. Res.*, *71*, 1033–1054, 1966.

Fritts, D. C., and L. Yuan, An analysis of gravity waves ducting in the atmosphere: Eckarts resonances in thermal and Doppler ducts, *J. Geophys. Res.*, *94*, 8455–8466, 1989.

Gardner, C. S., and D. G. Voelz, Lidar studies of the nighttime sodium layer over Urbana, Illinois, 2, Gravity waves, *J. Geophys. Res.*, *92*, 4673–4694, 1987.

Goodman, S. J., D. E. Buechler, P. D. Wright, and W. D. Rust. Lightning and precipitation history of a microburst producing storm, *Geophys. Res. Lett.*, *15*, 1185–1188, 1988.

Hecht, J. H., R. L. Walterscheid, D. C. Fritts, J. R. Isler, D. C. Senft, C. S. Gardner, and S. J. Franke, Wave breaking signatures in OH airglow and sodium densities and temperatures, 1, Airglow imaging, Na lidar, and MF radar observations, *J. Geophys. Res.*, *102*, 6655–6668, 1997.

Hecht, J. H., et al., A comparison of atmospheric tides inferred from observations at the mesopause during ALOHA-93 with the model predictions of the TIME-GCM, *J. Geophys. Res.*, *103*, 6307–6321, 1998.

Hedin, A. E., Extension of the MSIS model into the middle and lower atmosphere, *J. Geophys. Res.*, *96*, 1159, 1991.

Hedin, A. E., et al., Empirical wind model for the upper, middle, and lower atmosphere, *J. Atmos. Sol. Terr. Phys.*, *58*, 1421, 1996.

Hickey, M. P., G. Schubert, and R. L. Walterscheid, Gravity wave-driven fluctuations in the O_2 Atmospheric (0-1) nightglow from an extended, dissipative emission region, *J. Geophys. Res.*, *98*, 13,717–13,729, 1993.

Hickey, M. P., R. L. Walterscheid, M. J. Taylor, W. Ward, G. Schubert, Q. Zhou, F. Garcia, M. C. Kelley, and G. G. Shepherd, Numerical simulations of gravity waves imaged over Arecibo during the 10-day 1993 campaign, *J. Geophys. Res.*, *102*, 11,475–11,489, 1997.

Hickey, M. P., M. J. Taylor, C. S. Gardner, and C. R. Gibbons, Full-wave modeling of small-scale gravity waves using airborne lidar and observations of the Hawaiian airglow (ALOHA-93) $O(^1S)$ images and coincident Na wind, temperature lidar measurements, *J. Geophys. Res.*, *103*, 6439–6453, 1998.

Isler, J. R., M. P. Taylor, and D. J. Fritts, Observational evidence of wave ducting and evanescence in the mesosphere, *J. Geophys. Res.*, *102*, 26,301–26,313, 1997.

Larsen, M. F., Coqui 2: Mesospheric and lower thermospheric wind observations over Puerto Rico, *Geophys. Res. Lett.*, *27*(4), 445–448, 2000a.

Larsen, M. F., A shear instability seeding mechanism for quasi-periodic radar echos, *J. Geophys. Res.*, *105*, 24,931–24,940, 2000b.

McLandress, C., M. J. Alexander, and D. L. Wu, Microwave Limb Sounder observations of gravity waves in the stratosphere: A climatology and interpretation, *J. Geophys. Res.*, *105*, 11,947–11,967, 2000.

Nakamura, T., A. Higashikawa, T. Tsuda, and Y. Matsushita, Seasonal variations of gravity wave structures in OH airglow with a CCD imager at Shigaraki, *Earth Planets Space*, *51*, 897–906, 1999.

Pitteway, M. L. V., and C. O. Hines, The reflection and ducting of atmospheric gravity waves, *Can. J. Phys.*, *43*, 2222–2245, 1965.

Rosenberg, N. W., Statistical analysis of ionospheric winds, II, *J. Atmos. Sol. Terr. Phys.*, *30*, 907–917, 1968.

Schubert, G., M. P. Hickey, and R. L. Walterscheid, Gravity wave-driven fluctuations in OH nightglow from an extended dissipative emission region, *J. Geophys. Res.*, *96*, 13,869–13,880, 1991.

Senft, D. C., and C. S. Gardner, Seasonal variability of gravity wave activity and spectra in the mesopause region at Urbana, *J. Geophys. Res.*, *96*, 17,229–17,264, 1991.

She, C. Y., and R. P. Lowe, Seasonal temperature variations in the mesopause region at mid-latitude: Comparison of lidar and hydroxyl rotational temperatures using WINDII/UARS OH height profiles, *J. Atmos. Sol. Terr. Phys.*, *60*, 1573–1583, 1998.

States, R. J., and C. S. Gardner, Thermal structure of the mesopause region (80–105 km) at 40 N latitude, 1, Seasonal variations, *J. Atmos. Sci.*, *57*, 66–77, 2000.

Tai, K.-S., and Y. Ogura, An observational study of easterly waves over the eastern Pacific in the northern summer using FGGE data, *J. Atmos. Sci.*, *44*, 339–361, 1987.

Taylor, M. J., M. B. Bishop, and V. Taylor, All-sky measurements of short period gravity waves imaged in the OI(557.7 nm), Na (589,2 nm) and near infrared OH and O_2 (0,1) nightglow emissions during the ALOHA-93 campaign, *Geophys. Res. Lett.*, *22*, 2833–2836, 1995a.

Taylor, M. J., Y. Y. Gu, X. Tao, C. S. Gardner, and M. B. Bishop An investigation of intrinsic gravity wave signatures using coordinated lidar and nightglow image measurements, *Geophys. Res. Lett.*, *22*, 2853–2856, 1995b.

Tuan, T. F., and D. Tadic, A dispersion formula for analyzing model interferences among guided and free gravity modes and other phenomena in a realistic atmosphere, *J. Geophys. Res.*, *87*, 1648–1668, 1982.

Walterscheid, R. L., J. H. Hecht, R. A. Vincent, I. M. Reid, J. Woithe, and M. P. Hickey, Analysis and interpretation of airglow and radar observations of quasi-monochromatic gravity waves in the upper mesosphere and lower thermosphere over Adelaide, Australia (35 S, 138 E), *J. Atmos. Sol. Terr. Phys.*, *61*, 461–468, 1999.

Wang, D. Y., and T. F. Tuan, Brunt-Doppler ducting of small period gravity waves, *J. Geophys. Res.*, *93*, 9916–9926, 1988.

Wu, Q., and T. L. Killeen, Seasonal dependence of mesospheric gravity waves (<100 km) at Peach Mountain Observatory, Michigan. *Geophys. Res. Lett.*, *23*, 2211–2214, 1996.

J. H. Hecht and R. L. Walterscheid, Space Science Applications Laboratory, The Aerospace Corporation, M2-259, P. O. Box 92957, Los Angeles, CA 90009. (james.hecht@aero.org; richard.walterscheid@aero.org)

M. P. Hickey, Department of Physics and Astronomy, Clemson University, 308 Kinard Laboratory, Clemson, SC 29634. (hickey@hubcap.clemson.edu)

S. J. Franke, Department of Electrical and Computer Engineering, University of Illinois, 319 C.S.R.L, 1308 W. Main Street, Urbana, IL 61801. (franke@uiuc.edu)